Ideal type-I Weyl phonons in $BAsO_4$ with fewest Weyl points

Jian Liu [1,2] Xikui Ma,[3] Lei Sun,[3] Zeying Zhang,[4] Yun Ni,[1] Sheng Meng [5,6,*] and Mingwen Zhao [3,†]
[1] *School of Science, Hubei University of Technology, Wuhan 430068, China*
[2] *Shenzhen Research Institute of Shandong University, Shenzhen 518000, Guangdong, China*
[3] *School of Physics, Shandong University, Jinan 250100, China*
[4] *College of Mathematics and Physics, Beijing University of Chemical Technology, Beijing 100029, China*
[5] *Beijing National Laboratory of Condensed Matter Physics, and Institute of Physics, Chinese Academy of Sciences, Beijing 100190, China*
[6] *Songshan Lake Materials Laboratory, Dongguan, Guangdong 523808, China*

(Received 8 August 2023; accepted 22 December 2023; published 24 January 2024)

Weyl materials exhibit topologically nontrivial electronic or phonon energy-band crossings, offering promising conditions for fabricating novel topological devices and investigating exotic electrical and thermal transport properties. Here, we employ first-principles calculations to analyze the phonon dispersion of the experimentally synthesized boron arsenate ($BAsO_4$) material, revealing the presence of four ideal type-I Weyl points with topological charge $\mathcal{C} = \pm 1$ within the first Brillouin zone. These Weyl points are precisely located in the $k_z = 0.0$ plane and are constrained by the S_4 symmetry. Notably, both the O-atom and As-atom terminated surfaces exhibit clean and distinct surface arcs, connecting a pair of Weyl points with opposite chirality. These surface arcs maintain considerable separation in momentum space and span a length of approximately 0.687 Å^{-1}. Furthermore, we construct a three-band effective Hamiltonian to capture the Weyl-related phonon branches in $BAsO_4$ and to discuss the conditions governing the generation of Weyl points. Our results present an operational material platform for exploring the intrinsic properties of phononic Weyl-related phenomena.

DOI: 10.1103/PhysRevB.109.045203

I. INTRODUCTION

In recent years, Weyl phonon materials have attracted significant and ever-increasing interest, thanks to the unique aspect that phonons, being bosons, allow for the exploration of Weyl-related properties across the entire frequency range [1–18]. Weyl points represent a category of binary degenerate nodal points with chiral topological charges [19]. In three-dimensional (3D) crystals, the distribution of Berry curvature near the Weyl point in momentum space takes on a source and drain shape, resembling a magnetic monopole [20,21]. Importantly, when enclosing the Weyl point with a closed Gaussian surface to integrate the Berry curvature, the resulting topological charge is quantized, resulting in a topologically protected surface arc for the Weyl point [2,5,22–31]. According to the degree of tilt of the Weyl cone and whether it satisfies Lorentz symmetry [32], Weyl point can be classified into two types, type-I and type-II Weyl point, respectively. It is worth noting that ideal type-I Weyl materials tend to exhibit a characteristic of closed surface arcs [33], which holds particular interests for the design of relevant device.

At present, a major challenge in Weyl materials is the discovery of ideal Weyl points that exhibit a minimum number of Weyl points and clear, undisturbed topological surface arcs that are not obscured by clutter [33,34]. According to Nielsen-Ninomiya no-go theorem, there exists a net residual topological charge inside the Brillouin zone, necessitating at least one pair of Weyl points with opposite topological charges. The number of Weyl points is directly related to the presence of time-reversal symmetry, as the time-reversal symmetry operator transforms k to $-k$ without altering the chirality of Weyl points. Consequently, magnetic Weyl semimetallic materials can have a minimum number of Weyl points in electronic subsystem, precisely 2, because they break the time-reversal symmetry. In contrast, phonon systems preserve time-revisal symmetry, but the phonons do not need to satisfy Kramers degeneracy due to the time operator $\mathcal{T}^2 = 1$. Therefore, in Weyl phonon systems located at the time-reversal invariant point, there can also be only a single pair of Weyl points [35,36]. It should be mentioned that the corresponding topological charge of Weyl points must be even (2 and 4) [37–39]. Based on these insights, several Weyl phonon materials containing a single pair of Weyl points with topological charge of $\mathcal{C} = \pm 2$ or even $\mathcal{C} = \pm 4$ have been proposed [35,37]. However, for a Weyl phonon material with a charge $\mathcal{C} = \pm 1$, the minimum number of Weyl points contained in the Brillouin zone is still 4. The proposed Weyl phonon materials currently available with a topological charge of $\mathcal{C} = \pm 1$ often host numerous Weyl points. We believe Weyl phonon materials with odd topological charges and containing only 4 Weyl points are extremely rare.

Here, we predict that the $BAsO_4$ material exhibits ideal type-I Weyl phonons, characterizing by the presence of 4 accidentally degenerate Weyl points at approximately 22.9-THz

*smeng@iphy.ac.cn
†zmw@sdu.edu.cn

frequency. These four Weyl points have a topological charge of $\mathcal{C} = \pm 1$ and are on the $k_z = 0.0$ plane. The ideal characteristics of these Weyl points are as follows: (i) A Weyl phonon with a topological charge $\mathcal{C} = \pm 1$ must have a minimum number of 4 within the Brillouin zone; and (ii) The 4 Weyl points in the $BAsO_4$ material belong to the type-I class, and the bands away from these Weyl points do not intersect at the frequency of the Weyl point. The distance between the surface arcs that connect oppositely chiral Weyl points is measured to be 0.687 Å^{-1}. This leads to the formation of very clean surface arcs on the surface of the material, making $BAsO_4$ a promising candidate for the study of spin-1/2 Weyl-related phonon phenomena [40,41].

II. METHOD

First-principles calculations were performed at the density-functional theory level using the QUANTUM ESPRESSO (QE) package [42]. Projector augmented-wave pseudopotential was employed to model the electron-ion interaction, and the exchange-correlation function was in the form of generalized gradient approximation with Perdew-Burke-Ernzerhof [43]. The kinetic energy cutoff and the charge-density cutoff of the plane-wave basis were chosen to be 100 and 600 Ry, respectively. The lattice constants after full geometry optimization were adopted. The real-space interatomic force constants were calculated within density-functional perturbation theory [44] on a $4 \times 4 \times 4$ q mesh using the PHONON code in the QE package. The first-principles tight-binding Hamiltonian was constructed using the converged force constants and further imposed with the open-source software WANNIERTOOLS package [45] to calculate the Berry curvature, chirality, surface arc, and the nontrivial boundary-edges phonon states.

III. CRYSTAL STRUCTURE

The synthetic boron arsenate ($BAsO_4$) crystallizes in the $I\bar{4}$ space group (group No. 82) [46] and exhibits a fascinating combination of properties, including negative linear compressibility and negative Poisson's ratio [47,48]. The material $BAsO_4$ was first characterized by Schulze back in 1933 [49]. Its structural congener BPO_4 was prepared by solid-state reaction, with analytical-purity B_2O_3 and NH_4H_2-PO_4 in stoichiometric proportions [50]. The structural model of $BAsO_4$ can be found in Materials Project Database (part I of Supplemental Material) [51,52]. Each boron (or arsenic) atom is coordinated with 4 oxygen atoms to form the $[BO_4]$ (or $[AsO_4]$) tetrahedra. These tetrahedra units are interconnected by sharing corner oxygen atoms, creating a 3D open-framework structure. The optimized lattice constants for $BAsO_4$ are $a = 4.499$ and $c = 6.861$ Å, respectively, which agree well with the experimental data [49]. Figure 1(a) shows the structural model, with B, As, and O atoms occupying the $2c$, $2a$, and $8g$ Wyckoff positions, respectively. Space group No. 82 holds the S_4 point-group symmetry, which provides S_4 symmetry (the improper rotation $S_4 = IC_4$ is a proper fourfold rotation C_4 followed by inversion I), twofold rotation C_2, and the time-reversal symmetry, as generators at the Γ point. Figure 1(b) illustrates the high-symmetry points in the bulk Brillouin zone (BZ).

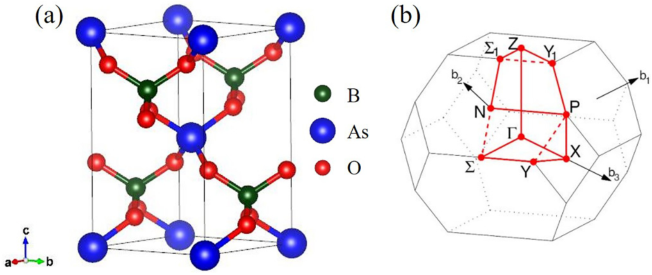

FIG. 1. Crystal structure and Brillouin zone (BZ). (a) The atomic structures of bulk $BAsO_4$. Green, blue, and red spheres denote the B, As, and O atoms, respectively. (b) The bulk BZ and the corresponding high-symmetry points.

IV. PHONON SPECTRUM

Figure 2 displays the phonon spectrum of $BAsO_4$, revealing no virtual frequency throughout the BZ, indicating the dynamic stability of the material. Since each primitive cell contains 6 atoms, the phonon spectrum consists of a total of 18 branches, including 3 acoustic branches and 15 optical branches. Notably, there is a noticeable band gap between the 11th phonon branch and the 12th phonon branch, with an indirect gap size of 4.067 THz. Additionally, the 12th and the 13th phonon branches appear to have a band crossing in the Γ-X direction, but exhibit a clear band gap in other high-symmetry paths, hinting at the potential presence of Weyl points [31]. We further calculated the phonon

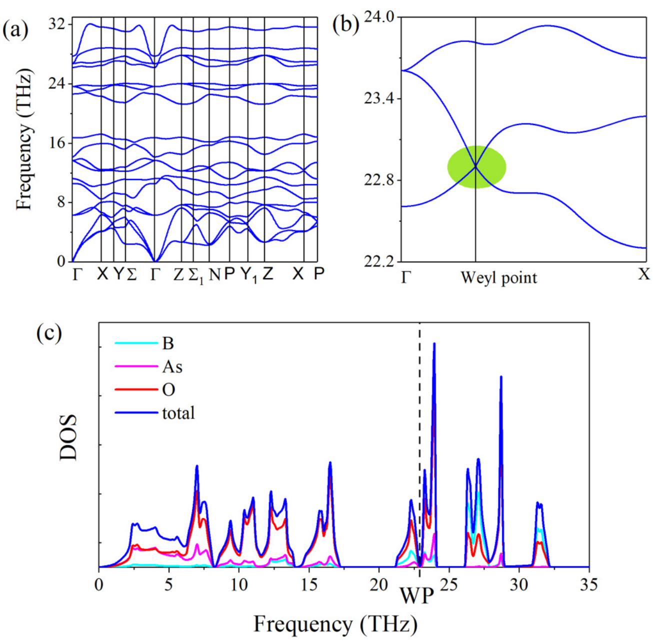

FIG. 2. Phonon dispersion of bulk $BAsO_4$: (a) Along the high-symmetry momentum path; and (b) along the Γ-Weyl point-X momentum path (the shape of the path is not a straight line). Only the Weyl-related phonon branches are displayed. (c) Atom-projected density of states (PDOS) of bulk $BAsO_4$. Total PDOS (blue lines) is the total contribution from those of B (cyan lines), As (pink lines), and O (red lines) atoms. The energy corresponding to the vertical black dotted line is the energy of the Weyl point.

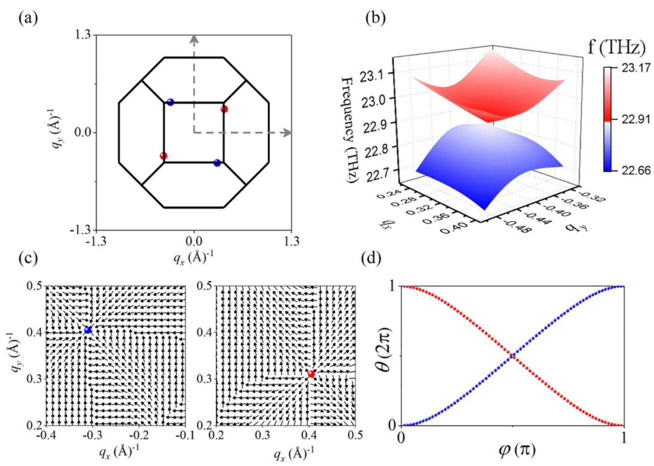

FIG. 3. (a) Top view from the [001] direction for the four Weyl points in the BZ. (b) Perspective plot of the phonon Weyl point (WP) in the $k_z = 0.0$ plane. (c) The distribution of normalized Berry curvature in the $k_z = 0.0$ plane. The blue and red spheres denote the Weyl points with negative and positive chirality, respectively. The length of each arrow is uniform and has no real meaning. (d) The evolution of the average position of Wannier centers for a WP with negative (blue squares) or positive chirality (red squares).

spectrum along the Γ-crossing point–X path and found that the nondegenerated band near the crossing point displays as linearly dispersive with a frequency of 22.9 THz. Analyzing the phonon density of states (DOS) as shown in Fig. 2(c), we identified that the phonon spectrum near the crossing point is mainly contributed by oxygen atoms, and the density of phonon states at the crossing points is extremely small, suggesting minimum hybridization with the bulk bands, thus indicating the ideal nature of the nodal point [33,34].

Further calculations have revealed the presence of four crossing points in the first BZ of the $BAsO_4$ material. These crossing points are situated in the $k_z = 0.0$ plane and their top-view distribution in the first BZ is illustrated in Fig. 3(a). One of the crossing points corresponds to the Cartesian coordinates (0.4049, 0.3113, 0.0) Å^{-1} [the corresponding fractional coordinates is (−0.0336, 0.0336, 0.2562)], while the other three points can be obtained via the S_4 symmetry. Detailed calculations of the phonon dispersion around the crossing points, as shown in Fig. 3(b), demonstrate linear dispersion in any direction within the $\{k_x, k_y\}$ direction, indicating that these crossing points form conelike structures. To characterize the topological properties of these crossing points, we have computed their Berry curvature distributions. As shown in Fig. 3(c), the Berry curvature near the crossing points forms a source and drainlike shape, reminiscent of that observed for a magnetic monopole [10,21,53]. In addition, by conducting closed-surface integrals of the Berry curvature near the crossing points, we calculated the topological charge for each of these crossing points. Figure 3(d) illustrates that each crossing point carries a topological charge of $\mathcal{C} = \pm 1$. Therefore, based on the dispersion relation, Berry curvature distribution, and topological charge analysis, we can confidently identify the four crossing points located in the $k_z = 0.0$ plane as Weyl points.

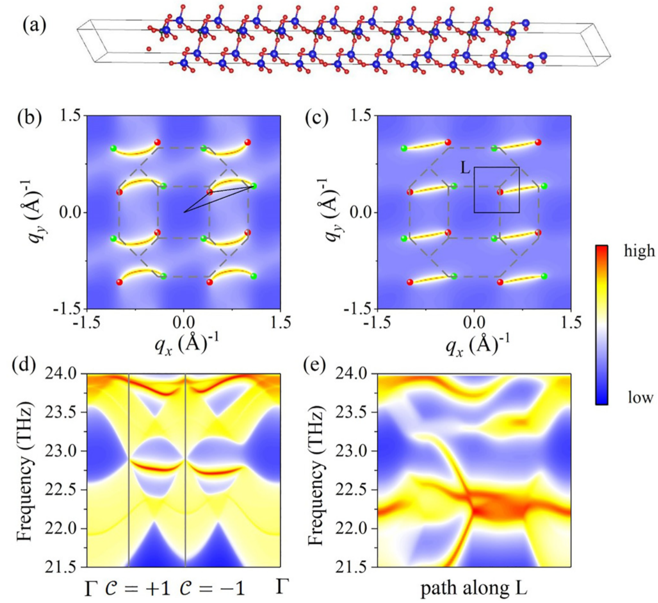

FIG. 4. (a) The schematic drawing of $BAsO_4$ slab model, where the left and right sides correspond to the O-atom and As-atom terminated surface, respectively. (b), (c) The momentum-resolved surface local density of states for $BAsO_4$ projected onto the O-atom (b) and As-atom (c) terminated surface. The red and green spheres denote the WPs with positive and negative chirality, respectively. The dashed gray border represents the top view of BZ in the [001] direction. (d) Surface band structure along the momentum path Γ-WP-WP-Γ [denoted by a black triangle in (b)]. (e) The same as panel (d), but for the momentum path L [denoted by a black rectangle in (c)].

Similar to the Fermi arcs observed in Weyl semimetals, Weyl phonons also exhibit topologically protected surface states that connect oppositely chiral Weyl points in momentum space [54]. To investigate these surface states, we constructed a 50-layer-thick model to calculate the topological surface states at the (001) surface of the $BAsO_4$ material, as shown in Fig. 4(a). Subsequently, we examined the surface phonon-state densities of the O (oxygen atom)-terminated surface [Fig. 4(b)] and the As-terminated surface [Fig. 4(c)] at a fixed frequency of 22.9 THz. Since $BAsO_4$ lacks central inversion symmetry, the surface states on the O-terminated surface and As-terminated surface are different. However, in both cases, clear surface arcs can be observed in momentum space, connecting the Weyl points (WPs) with opposite chirality in momentum space. The splitting distance of a pair of WPs connected by surface arcs is 0.687 Å^{-1}, which is equivalent to 41.12% of the in-plane reciprocal lattice constants. These long and clean surface arcs are advantageous for experimental measurements of topological surface states and are significant for the application of topological quantum transport of surface phonons.

In addition to the surface phonon-state densities, we further calculated the spectral function of the surface phonon on the As-terminated surface as shown in Figs. 4(d) and 4(e): (i) When the momentum path follows the direction from Γ to the Wey point with a topological charge of $\mathcal{C} = +1$, then to the Weyl point with a topological charge of $\mathcal{C} = -1$, and finally back to Γ, we clearly observe a topological nontrivial surface state connecting two Weyl points in the energy space; and (ii) When the momentum path is closed and contains only one Weyl point, resulting in a net enclosed topological charge of 1, we observe a topologically nontrivial state similar to that found in the quantum anomalous Hall effect [23,55,56]. This state connects the upper branch of the Weyl point (analogous to the conduction band in electronic systems) with the lower branch of the Weyl point (analogous to the valence band). The analysis of the spectral function of surface phonons provides valuable insights into the unique topological surface states of the $BAsO_4$ material, which are vital for understanding its exotic phonon phenomena and exploring potential applications in topological quantum transport of surface phonons.

Indeed, the Weyl phonons observed in the $BAsO_4$ system meet the criteria of ideal Weyl points, as defined in the literature [33,34,57–59]. (i) The bands far from the Weyl point do not intersect in the energy range around the frequency $f = 22.9$ THz, as shown in Figs. 2(b) and 2(c). The phonon DOS at the Weyl frequency corresponds to an extremely small density of states, indicating a clear absence of band crossings; (ii) The surface phonon DOS in momentum space, as well as the surface phonon spectral function in energy space, as depicted in Fig. 4, exhibit topologically nontrivial surface arcs and states that are free from clutter; and (iii) According to the Nielsen-Ninomiya no-go theorem, for a Weyl phonon with time-reversal symmetry, the minimum number of Weyl points in the first BZ is 4 if the corresponding topological charge is not even [35,37]. In the case of $BAsO_4$, we have identified 4 Weyl points with a topological charge of $\mathcal{C} = \pm 1$, indicating that it is an ideal type-I Weyl phonon material containing the fewest Weyl points with this specific topological charge.

V. SYMMETRY ANALYSIS AND EFFECTIVE MODEL

At the Γ point, space group No. 82 holds the S_4 point-group symmetry, which is generated by twofold rotation symmetry C_2, S_4 and time-reversal symmetry. The transformations of momentum k under the generating operators are as follows:

$$C_2 : (k_x,\ k_y, k_z) \rightarrow (-k_x - k_z,\ -k_y - k_z,\ k_z) \quad (1)$$

$$S_4 : (k_x,\ k_y,\ k_z) \rightarrow (k_y + k_z,\ -k_x,\ -k_z)$$

We construct an effective Hamiltonian under the constraint of

$$D(g)H(k)D^{+}(g) = H(gk) \quad (2)$$

for the symmetry operation g and its representation $D(g)$ [60]. Based on our first-principles calculations, we find that the upper and lower parts of the Weyl cone belong to the two-dimensional representation E and the one-dimensional representation A, respectively. Considering three bands as the basis in the effective Hamiltonian, the basis at the Γ point can be written as $\{k_x + ik_y,\ k_x - ik_y\}$ for E representation and $\{k_x^2 + k_y^2\}$ for A representation. The corresponding 3D representations of the above symmetry operators in the basis are given by

$$D(C_2) = \begin{pmatrix} 1 & 0 & 0 \\ 0 & -1 & 0 \\ 0 & 0 & -1 \end{pmatrix},\quad D(S_4) = \begin{pmatrix} 1 & 0 & 0 \\ 0 & -i & 0 \\ 0 & 0 & i \end{pmatrix}. \quad (3)$$

Using the representation matrices, we can then construct a three-bands $k \cdot p$ model in the $k_z = 0.0$ plane [61]. The most general three-band effective Hamiltonian up to $O(k^2)$ near the Γ point can be written as

$$H_{\text{eff}} = c_1(g_1k_+ - g_2k_-) + c_2(g_4k_+ - g_5k_-) + c_3g_3k_\parallel^2 + c_4g_8k_\parallel^2 + H_\varepsilon, \quad (4)$$

where $H_\varepsilon = diag(\varepsilon_0,\ \varepsilon_0,\ \varepsilon_1)$, $\varepsilon_{0,\ 1}$ are the energy constant terms, $c_i(i = 1, 2, 3, 4)$ are real parameters, $g_i(i = 1, \ldots, 8)$ are eight Gell-Mann matrices (part II of Supplemental Material) [52], $k_\parallel^2 = k_x^2 + k_y^2$, and $k_\pm = k_x \pm ik_y$. By plugging the Gell-Mann matrices into the Hamiltonian H_{eff}, its matrix form takes

$$H_{\text{eff}} = \begin{bmatrix} d_1k_\parallel^2 + \varepsilon_0 & c_1(k_+ + ik_-) & c_2(k_+ + ik_-) \\ c_1(k_+ - ik_-) & d_2k_\parallel^2 + \varepsilon_0 & 0 \\ c_2(k_+ - ik_{-\_}) & 0 & d_3k_\parallel^2 + \varepsilon_1 \end{bmatrix}, \quad (5)$$

where $d_1 = c_3 + \frac{c_4}{\sqrt{3}}$, $d_2 = -c_3 + \frac{c_4}{\sqrt{3}}$, $d_3 = \frac{-2c_4}{\sqrt{3}}$. If we ignore the second- and higher orders of momentum k in H_{eff}, the Hamiltonian can be simplified to a typical Hamiltonian of spin-1/2 Weyl points [54]:

$$H'_{\text{eff}} = \begin{bmatrix} \varepsilon_0 & c_1(k_+ + ik_-) & c_2(k_+ + ik_-) \\ c_1(k_+ - ik_-) & \varepsilon_0 & 0 \\ c_2(k_+ - ik_-) & 0 & \varepsilon_1 \end{bmatrix}. \quad (6)$$

The eigenvalue (E) equation of this matrix is

$$(-E + \varepsilon_0)^2(-E + \varepsilon_1) - \left[(-E + \varepsilon_0)c_2^2 + (-E + \varepsilon_1)c_1^2\right] \times 2\left(k_x^2 - k_y^2\right) = 0. \quad (7)$$

When the condition $k_x^2 - k_y^2 = 0$ is met, the three eigenvalues of this matrix are $E_1 = \varepsilon_1$ and $E_{2,3} = \varepsilon_0$, which gives four crossing points and supports the existence of spin-1/2 Weyl points in the $BAsO_4$ material [54]. The parameters in the three-band effective Hamiltonian can be obtained by fitting the energy-band results calculated from the first-principles calculations (part III of Supplemental Material) [52].

VI. CONCLUSION

In conclusion, our theoretical analyses have demonstrated that $BAsO_4$ features 4 ideal type-I Weyl phonons on the $k_z = 0$ plane. These 4 Weyl points are accidentally degenerate and are connected to each other through S_4 symmetry, with a topological charge of $\mathcal{C} = \pm 1$. Importantly, the bands near the Weyl nodes show minimal hybridization with the bulk bands, resulting in distinguishable surface states on the O-terminated and As-terminated surfaces. Furthermore, the Nielsen-Ninomiya no-go theorem dictates that if the topological charge of a Weyl point is not even, the minimum number of Weyl phonon points in the first BZ is 4. $BAsO_4$ not only possesses the lowest number of Weyl points ($\mathcal{C} = \pm 1$), but also exhibits clean surface arcs, making it a highly promising platform for realizing phonon topological effects and studying Weyl-related phonon phenomenon. The exceptional properties of $BAsO_4$ as an ideal type-I Weyl phonon material positions it as a compelling candidate for extensive research and promising applications in the realm of topological phononics.

ACKNOWLEDGMENTS

J.L. acknowledges financial support from the Shenzhen Science and Technology Program (Grant No. RCBS20200714114908126), National Natural Science Foundation Youth Fund (Grant No. 12304538), and School level research project of Hubei University of Technology (Grant No. XJ2022000901). Z.Z. acknowledges the support by the NSF of China (Grant No. 12004028). S.M. acknowledges support by the National Natural Science Foundation of China (Grant No. 12025407). M.Z. acknowledges support by the National Natural Science Foundation of China (Grant No. 12074218) and the Taishan Scholar Program of Shandong Province.

The authors declare no competing financial interest.

[1] M. Gao, W. Zhang, and L. Zhang, Nondegenerate chiral phonons in graphene/hexagonal boron nitride heterostructure from first-principles calculations, Nano Lett. **18**, 4424 (2018).

[2] F. Li, X. Huang, J. Lu, J. Ma, and Z. Liu, Weyl points and Fermi arcs in a chiral phononic crystal, Nat. Phys. **14**, 30 (2017).

[3] V. Peri, M. Serra-Garcia, R. Ilan, and S. D. Huber, Axial-field-induced chiral channels in an acoustic Weyl system, Nat. Phys. **15**, 357 (2019).

[4] J. Li, Q. Xie, J. Liu, R. Li, M. Liu, L. Wang, D. Li, Y. Li, and X.-Q. Chen, Phononic Weyl nodal straight lines in MgB_2, Phys. Rev. B **101**, 024301 (2020).

[5] Y. Liu, N. Zou, L. Zhao, X. Chen, Y. Xu, and W. Duan, Ubiquitous topological states of phonons in solids: Silicon as a model material, Nano Lett. **22**, 2120 (2022).

[6] J. Wang, H. Yuan, Y. Liu, F. Zhou, X. Wang, and G. Zhang, Hourglass Weyl and Dirac nodal line phonons, and drumhead-like and torus phonon surface states in orthorhombic-type KCuS, Phys. Chem. Chem. Phys. **24**, 2752 (2022).

[7] M. Zhong, H. Liu, J. Wang, C. Xie, H. Yuan, Z. Zhang, X. Wang, and G. Zhang, Accurate recipe for predicting valley linear Weyl phonons in two dimensions, arXiv:2302.01054.

[8] M. D. Liberto, A. Kruckenhauser, P. Zoller, and M. A. Baranov, Topological phonons in arrays of ultracold dipolar particles, Quantum **6**, 731 (2022).

[9] D. Campi, S. Kumari, and N. Marzari, Prediction of phonon-mediated superconductivity with high critical temperature in the two-dimensional topological semimetal W_2N_3, Nano Lett. **21**, 3435 (2021).

[10] J. Li, J. Liu, S. A. Baronett, M. Liu, L. Wang, R. Li, Y. Chen, D. Li, Q. Zhu, and X.-Q. Chen, Computation and data driven discovery of topological phononic materials, Nat. Commun. **12**, 1204 (2021).

[11] G. F. Lange, A. Bouhon, B. Monserrat, and R.-J. Slager, Topological continuum charges of acoustic phonons in two dimensions and the Nambu-Goldstone theorem, Phys. Rev. B **105**, 064301 (2022).

[12] J. Li, Q. Xie, S. Ullah, R. Li, H. Ma, D. Li, Y. Li, and X.-Q. Chen, Coexistent three-component and two-component Weyl phonons in TiS, ZrSe, and HfTe, Phys. Rev. B **97**, 054305 (2018).

[13] G. Liu, Y. Jin, Z. Chen, and H. Xu, Symmetry-enforced straight nodal-line phonons, Phys. Rev. B **104**, 024304 (2021).

[14] Q.-B. Liu, H.-H. Fu, and R. Wu, Topological phononic nodal hexahedron net and nodal links in the high-pressure phase of the semiconductor CuCl, Phys. Rev. B **104**, 045409 (2021).

[15] Q.-B. Liu, Z. Wang, and H.-H. Fu, Charge-four Weyl phonons, Phys. Rev. B **103**, L161303 (2021).

[16] X. Wang, T. Yang, Z. Cheng, G. Surucu, J. Wang, F. Zhou, Z. Zhang, and G. Zhang, Topological nodal line phonons: Recent advances in materials realization, Appl. Phys. Rev. **9**, 041304 (2022).

[17] Y. Yang, F. Zhou, J. Wang, Y. Liu, Y. Cui, G. Ding, and X. Wang, Unpaired Weyl phonon systems in $NaHPO_3NH_2$, Appl. Phys. Lett. **122**, 232202 (2023).

[18] Y. Yang, J. Wang, Y. Liu, Y. Cui, G. Ding, and X. Wang, Topological phonons in Cs-Te binary systems, Phys. Rev. B **107**, 024304 (2023).

[19] Y. Chen, Y. Xie, S. A. Yang, H. Pan, F. Zhand, M. L. Cohen, and S. Zhang, Nanostructured carbon allotropes with Weyl-like loops and points, Nano Lett. **15**, 6974 (2015).

[20] J. Im, C. H. Kim, and H. Jin, Ferroelectricity-driven phonon Berry curvature and nonlinear phonon Hall transports, Nano Lett. **22**, 8281 (2022).

[21] R. Wang, B. W. Xia, Z. J. Chen, B. B. Zheng, Y. J. Zhao, and H. Xu, Symmetry-protected topological triangular Weyl complex, Phys. Rev. Lett. **124**, 105303 (2020).

[22] D.-S. Tang and B.-Y. Cao, Topological effects of phonons in GaN and AlGaN: A potential perspective for tuning phonon transport, J. Appl. Phys. **129**, 085102 (2021).

[23] Q.-B. Liu, Z.-Q. Wang, and H.-H. Fu, Topological phonons in allotropes of carbon, Mater. Today Phys. **24**, 100694 (2022).

[24] Y. H. Yang, Z. Gao, X. L. Feng, Y. X. Huang, P. H. Zhang, S. A. Yang, Y. D. Chong, and B. L. Zhang, Ideal Unconventional Weyl Point in a Chiral Photonic Metamaterial, Phys. Rev. Lett. **125**, 143001 (2020).

[25] Z.-K. Ding, Y.-J. Zeng, H. Pan, N. Luo, J. Zeng, L.-M. Tang, and K.-Q. Chen, Edge states of topological acoustic phonons in graphene zigzag nanoribbons, Phys. Rev. B **106**, L121401 (2022).

[26] Y. J. Jin, Z. J. Chen, X. L. Xiao, and H. Xu, Tunable double Weyl phonons driven by chiral point group symmetry, Phys. Rev. B **103**, 104101 (2021).

[27] P. C. Sreeparvathy, C. Mondal, C. K. Barman, and A. Alam, Coexistence of multifold and multidimensional topological phonons in $KMgBO_3$, Phys. Rev. B **106**, 085102 (2022).

[28] J.-Y. You, X.-L. Sheng, and G. Su, Topological gimbal phonons in T-carbon, Phys. Rev. B **103**, 165143 (2021).

[29] T. Zhang, R. Takahashi, C. Fang, and S. Murakami, Twofold quadruple Weyl nodes in chiral cubic crystals, Phys. Rev. B **102**, 125148 (2020).

[30] F. Zhou, H. Chen, Z.-M. Yu, Z. Zhang, and X. Wang, Realistic cesium fluogermanate: An ideal platform to realize the topologically nodal-box and nodal-chain phonons, Phys. Rev. B **104**, 214310 (2021).

[31] M. Zhong, Y. Han, J. Wang, Y. Liu, X. Wang, and G. Zhang, Material realization of double-Weyl phonons and phononic double-helicoid surface arcs with P_{213} space group, Phys. Rev. Mater. **6**, 084201 (2022).

[32] A. A. Soluyanov, D. Gresch, Z. Wang, Q. Wu, M. Troyer, X. Dai, and B. A. Bernevig, Type-II Weyl semimetals, Nature (London) **527**, 495 (2015).

[33] J. Ruan, S. K. Jian, H. Yao, H. Zhang, S. C. Zhang, and D. Xing, Symmetry-protected ideal Weyl semimetal in HgTe-class materials, Nat. Commun. **7**, 11136 (2016).

[34] B. W. Xia, R. Wang, Z. J. Chen, Y. J. Zhao, and H. Xu, Symmetry-protected ideal type-II Weyl phonons in CdTe, Phys. Rev. Lett. **123**, 065501 (2019).

[35] X. Wang, F. Zhou, Z. Zhang, W. Wu, Z.-N. Yu, and S. Yang, Single pair of multi-Weyl points in nonmagnetic crystals, Phys. Rev. B **106**, 195129 (2022).

[36] G. Ding, C. Xie, J. Bai, Z. Cheng, X. Wang, and W. Wu, Recipe for single-pair-Weyl-points phonons carrying the same chiral charges, Phys. Rev. B **108**, L020302 (2023).

[37] Z.-Q. Wang, Q.-B. Liu, X.-F. Yang, and H.-H. Fu, Single-pair Weyl points with the maximum charge number in acoustic crystals, Phys. Rev. B **106**, L161302 (2022).

[38] G. Ding, C. Xie, J. Gong, J. Wang, J. Bai, W. Wang, D. Li, X.-P. Li, and X. Wang, Exotic topological phonon modes in semiconductors: Symmetry analysis and first-principles calculations for representative examples, Phys. Rev. B **108**, 075201 (2023).

[39] Y. Yang, C. Xie, Y. Cui, X. Wang, and W. Wu, Maximally charged single-pair multi-Weyl point phonons in P_{23}-type BeH_2, Phys. Rev. B **107**, 054310 (2023).

[40] H. Liu, M. Zhong, and M. Ju, Prediction of phonon-mediated superconductivity and topological surface states in $NbRu_3C$, Physica B **646**, 414255 (2022).

[41] P.-F. Liu, J. Li, C. Zhang, X.-H. Tu, J. Zhang, P. Zhang, B.-T. Wang, and D. J. Singh, Type-II Dirac cones and electron-phonon interaction in monolayer biphenylene from first-principles calculations, Phys. Rev. B **104**, 235422 (2021).

[42] P. Giannozzi, S. Baroni, N. Bonini, M. Calandra, R. Car, C. Cavazzoni, D. Ceresoli, G. L. Chiarotti, M. Cococcioni, I. Dabo *et al.*, QUANTUM ESPRESSO: A modular and open-source software project for quantum simulations of materials, J. Phys.: Condens. Matter **21**, 395502 (2009).

[43] J. Perdew, K. Burke, and M. Ernzerhof, Generalized gradient approximation made simple, Phys. Rev. Lett. **77**, 3865 (1996).

[44] S. Baroni, S. Gironcoli, A. D. Corso, and P. Giannozzi, Phonons and related crystal properties from density-functional perturbation theory, Rev. Mod. Phys. **73**, 515 (2001).

[45] Q. Wu, S. Zhang, H.-F. Song, M. Troyer, and A. A. Soluyanov, WannierTools: An open-source software package for novel topological materials, Comput. Phys. Commun. **224**, 405 (2018).

[46] J. Haines, C. Chateau, J. M. Leger, C. Bogicevic, S. Hull, D. D. Klug, and J. S. Tse, Collapsing cristobalitelike structures in silica analogues at high pressure, Phys. Rev. Lett. **91**, 015503 (2003).

[47] J. Dagdelen, J. Montoya, M. Jong, and K. Persson, Computational prediction of new auxetic materials, Nat. Commun. **8**, 323 (2017).

[48] J. N. Grima-Cornish, L. Vella-Żarb, and J. N. Grima, Negative linear compressibility and auxeticity in boron arsenate, Ann. Phys. (Berlin, Ger.) **532**, 1900550 (2020).

[49] G. E. R. Schulze, Die Kristallstruktur von BPO_4 und $BAsO_4$, Naturwissenschaften **21**, 562 (1933).

[50] Z. Li, Z. Lin, Y. Wu, P. Fu, Z. Wang, and C. Chen, Crystal growth, optical properties measurement, and theoretical calculation of BPO_4, Chem. Mater. **16**, 2906 (2004).

[51] A. Jain, S. P. Ong, G. Hautier, W. Chen, W. D. Richards, S. Dacek, S. Cholia, D. Gunter, D. Skinner, G. Ceder, and K. A. Persson, Commentary: The Materials Project: A materials genome approach to accelerating materials innovation, APL Mater. **1**, 011002 (2013).

[52] See Supplemental Material at http://link.aps.org/supplemental/10.1103/PhysRevB.109.045203 for more details about the cell parameters of BAsO4 and the format of eight Gell-Mann matrices.

[53] J. Wang, H. Yuan, W. Wang, G. Ding, X.-P. Li, and X. Wang, Fully spin-polarized hourglass charge-three Weyl points and sextuple-helicoid surface arcs in $P6_322$-type $BaNiIO_6$, Phys. Rev. B **108**, 054424 (2023).

[54] T. Zhang, Z. Song, A. Alexandradinata, H. Weng, C. Fang, L. Lu, and Z. Fang, Double-Weyl phonons in transition-metal monosilicides, Phys. Rev. Lett. **120**, 016401 (2018).

[55] J. Liu, S. Meng, and J. T. Sun, Spin-orientation-dependent topological states in two-dimensional antiferromagnetic $NiTl_2S_4$ monolayers, Nano Lett. **19**, 3321 (2019).

[56] J. Li, Y. Li, S. Du, Z. Wang, B. Gu, S.-C. Zhang, K. He, W. Duan, and Y. Xu, Intrinsic magnetic topological insulators in van der Waals layered $MnBi_2Te_4$-family materials, Sci. Adv. **5**, eaaw5685 (2019).

[57] J. Liu, W. Hou, E. Wang, S. Zhang, J.-T. Sun, and S. Meng, Ideal type-II Weyl phonons in wurtzite CuI, Phys. Rev. B **100**, 081204(R) (2019).

[58] P.-F. Liu, J. Li, X.-H. Tu, H. Li, J. Zhang, P. Zhang, Q. Gao, and B.-T. Wang, First-principles prediction of ideal type-II Weyl phonons in wurtzite ZnSe, Phys. Rev. B **103**, 094306 (2021).

[59] X. Wang, F. Zhou, T. Yang, M. Kuang, Z.-M. Yu, and G. Zhang, Symmetry-enforced ideal lanternlike phonons in the ternary nitride Li_6WN_4, Phys. Rev. B **104**, L041104 (2021).

[60] Z. Zhang, Z.-M. Yu, G.-B. Liu, Z. Li, S. Yang, and Y. Yao, MagneticKP: A package for quickly constructing k·p models of magnetic and non-magnetic crystals, Comput. Phys. Commun. **290**, 108784 (2023).

[61] C.-X. Liu, X.-L. Qi, H. Zhang, X. Dai, Z. Fang, and S.-C. Zhang, Model Hamiltonian for topological insulators, Phys. Rev. B **82**, 045122 (2010).